CCS Chemistry

RESEARCH ARTICLE

Received: Oct. 4, 2022 | Accepted: Dec. 7, 2022 | Published: Jan. 5, 2023

Atomic Bridging of Sn Single Atom with Nitrogen and Oxygen Atoms for the Selective Electrocatalytic Reduction of CO_2

Bari Wulan[1], Xueying Cao[1], Dongxing Tan[1], Xinxin Shu[1], Jizhen Ma[1], Shaoqi Hou[2] & Jintao Zhang[1]*

[1]*Key Laboratory for Colloid and Interface Chemistry of State Education Ministry, School of Chemistry and Chemical Engineering, Shandong University, Jinan 250100,* [2]*School of Mathematical and Physical Sciences, University of Technology Sydney, Ultimo, New South Wales 2007*

**Corresponding author: jtzhang@sdu.edu.cn*

Cite this: *CCS Chem.* **2023**, 5, 2415–2425
DOI: 10.31635/ccschem.022.202202464

The atomic coordination structure of single atom catalysts is crucial in modulating the electrocatalytic reduction of CO_2 into desirable products. However, there remains limited insight into their roles and catalytic mechanisms. In comparison with commonly proposed metal-N_4 moieties, herein the atomic bridging structure of nitrogen-tin-oxygen confined in porous carbon fibers is first presented for the selective reduction of CO_2. With the detailed identification of such a unique structure, the in situ experimental results and theoretical calculations demonstrate that the bridging structure with reactive oxygen species enables the favorable surface electronic status to form adsorbed intermediate, *COOH for selective CO generation. Typically, the electrocatalyst displays high Faradaic efficiency in reducing CO_2 into CO, but formate is produced on traditional Sn-based catalysts. Additionally, the solar-driven CO_2-H_2O system displays a desirable solar-to-CO conversion efficiency of 12.9%. This work provides fundamental guidance for the rational regulation of the atomic coordination structure to improve the production selectivity.

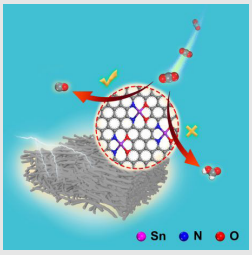

The nitrogen-tin-oxygen (N_2-Sn-O_2) moieties confined in porous carbon fiber structure exhibit good catalytic activity and selectivity for CO generation with high Faradaic efficiency.

Keywords: **electrocatalysis, atomic bridging structure, nitrogen-tin-oxygen, solar energy, selectivity**

Introduction

The severe energy crisis and increasing levels of CO_2 in the atmosphere, along with the excessive consumption of fossil fuels, has stimulated the development of carbon capture, utilization, and storage technologies.[1–4] Electrochemical conversion of CO_2 into valuable compounds has attracted much attention because of the mild reaction conditions and potentially valuable products. Specifically, it shows great potential to be coupled with renewable energy sources such as wind and solar energy, offering a promising strategy to achieve the goals of a carbon-neutral cycle and pollutant reduction.[5–11] However, the reduction of carbon dioxide with a thermodynamic uphill pathway to forming the key intermediate, $CO_2^{\bullet-}$, is inevitably hindered by the competitive hydrogen evolution

reaction (HER), resulting in poor conversion efficiency.[12–14] Noble metal catalysts (e.g., Au, Ag, and Pd) can efficiently convert CO_2 to CO, but are severely constrained by the scarcity and high cost.[15–17] Therefore, the rational design of low cost and efficient electrocatalysts with good selectivity and catalytic activity is of great significance, but still challenging.

The atomic dispersion of metal atoms on a conductive carbon matrix with tunable coordination structures provides promising platforms for the precise design of advanced electrocatalysts to enhance the carbon dioxide reduction reaction (CO_2RR).[18,19] It provides a large promising space to adjust the coordination environment and species for regulating the surface electronic interaction between intermediates and coordination species, thereby enabling electrocatalytic activity and production selectivity.[20–22] Transition metal-based single-atom catalysts with metal-nitrogen-carbon moieties (e.g., Fe-N-C, Co-N-C, Ni-N-C, and Zn-N-C)[23–26] feature unique electronic structures with optimized d-band centers that effectively affect the antibonding interactions between active sites and adsorbates for improved Faradaic efficiency. Notably, single-atom catalysts with main group elements such as Sb and Sn are considered the most promising catalysts to generate favorable adsorbed intermediates, *HCOO, for the reduction of CO_2 into formate. The coordination of antimony with nitrogen was observed to form Sb-N_4 sites, which could efficiently produce formate due to the optimized adsorption energy to the intermediates.[27] Xie et al.[28] found that the Sn quantum sheets confined among graphene sheets with a low Sn–Sn coordination structure enabled the strong adsorption of intermediate ($CO_2^{\bullet-}$) for formate production. Moreover, the positively charged $Sn^{\delta+}$ of Sn-N_2-C_2 has been revealed to accelerate the protonation process via $CO_2^{\bullet-}$ and *HCOO stabilization.[29] Therefore, the coordination of Sn with nitrogen generally enables the generation of formate as the predominant product due to the specific electronic status and thermodynamic difficulty in the formation of CO. Specifically, the limited insight into the reaction mechanism restricts the coordination structure design to optimize the selective product generation.[27,30,31] Additionally, it is still debated whether the surface oxide layer will change the electrocatalytic activities of tin species for carbon dioxide reduction.

With the above consideration, herein, as a proof-of-concept, we demonstrated the ability to atomically disperse Sn species in a nitrogen-doped carbon matrix with a goal of modulating the unique coordination structure to enhance selective electrocatalysis via a facile in situ polymerization-pyrolysis method. Impressively, the synchrotron-radiation X-ray absorption fine structure (XAFS) and aberration-corrected high-angle annular dark-field scanning transmission electron microscopy (HAADF-STEM) identified the novel atomic bridging structure of tin with two nitrogen and two oxygen atoms (nitrogen-tin-oxygen [N_2-Sn-O_2]) for the first time, to the best of our knowledge. The optimized Sn-NMC-1000 displayed good CO_2 electroreduction performance with a high Faradaic efficiency of 92.1% for CO, which is different from most reported Sn-based electrocatalysts. Density functional theory (DFT) calculations and in-situ characteristic results revealed the crucial role of N_2-Sn-O_2 moieties in regulating the electronic structure to tailor the intermediate adsorption process with the lowest reaction barrier. Thus, the rate-determining step is shifted from adsorbed intermediate *HCOOH into *COOH for the predominant generation of CO. Uncovering the relationship between the unique coordination structure of tin with nitrogen and oxygen atoms is highly crucial to the rational design of advanced electrocatalysts to regulate electrocatalytic activity and product selectivity by applying basic principles. More interestingly, a solar-driven CO_2-H_2O system was fabricated with the as-prepared electrocatalysts to achieve the desirable solar-to-CO conversion efficiency of 12.9%. This work provides a novel strategy for the rational design of coordination structures to tailor the product distribution.

Experimental Methods

Methods

In a typical procedure, 2 mL aniline monomer was added into 25 mL 2 M HCl solution with 0.05 mmol of $SnCl_2$ under stirring to form the transparent solution. After cooling to 4 °C, 1 mL H_2O_2 (30 vol %) was poured into the mixture and maintained for 24 h. The resultant precipitants were collected by thoroughly washing with deionized (DI) water and freeze-drying overnight. The obtained samples were annealed at different temperatures (900, 1000, and 1100 °C) in N_2 atmosphere, denoted as Sn-NMC-900, Sn-NMC-1000, and Sn-NMC-1100, respectively. The 0.25Sn-NMC-1000 and 0.5Sn-NMC-1000 were synthesized by a similar procedure except that the addition of $SnCl_2$ was increased to 0.25 and 0.5 mmol. The same procedure was used to synthesize the NMC-1000 in the absence of $SnCl_2$.

Electrochemical measurements

The electrocatalytic CO_2 reduction reaction was carried out on an CHI760e workstation in the H-type cell with a three-electrode system including a working electrode, a platinum foil counter electrode, and an Ag/AgCl reference electrode, which was separated by a proton exchange membrane (Nafion 117). The as-prepared catalyst was loaded on carbon fiber with a mass loading of 1 mg cm^{-2}. All potentials were referred to the reversible hydrogen electrode (RHE) ($E_{RHE} = E_{Ag/AgCl} + 0.059 \times pH + 0.198$). The electrochemical active surface area (ECSA) was estimated by conducting electrochemical

DOI: 10.31635/ccschem.022.202202464
Citation: *CCS Chem.* **2023**, 5, 2415–2425
Link to VoR: https://doi.org/10.31635/ccschem.022.202202464

double-layer capacitance (C_{dl}) in a non-Faradaic potential range. The electrochemical impedance spectroscopy (EIS) was conducted over a frequency range from 100 to 1 kHz at a potential of −0.8 V in CO_2-saturated electrolyte. The gaseous products (Supporting Information Figure S1a) in the cathode chamber were vented directly into the gas sampling loop of a gas chromatography (GC 7920) equipped with Molsieve 5A column and a thermal conductivity detector. The Faradaic efficiency of gaseous products can be calculated using the following equation:

$$FE(\%) = \frac{Q_{CO}}{Q_{tot}} \times 100\% = \frac{\left(\frac{v}{60\ s/min}\right) \times \left(\frac{x}{24{,}000 cm^3/mol}\right) \times N \times F}{J} \times 100\% \quad (1)$$

where v is the flow rate of CO_2, x is the concentration of gaseous products in the sample-loop, N is the number of molecules for desired products, F is the Faraday constant (96,500 C mol^{-1}), and J is the steady-state current.

The liquid products (Supporting Information Figure S1b) were quantified by a high-performance liquid chromatograph equipped with a Bio-Rad HPX-87H column and ultraviolet–visible detector. The products were evaluated according to the calibration curves based on the dilution of standard products, and the corresponding Faradaic efficiency can be calculated as below:

$$FE(\%) = \frac{\alpha n F}{Q} \quad (2)$$

where α is the number of electrons required to form targeted products (e.g., α = 2 for reduction CO_2 to HCOOH or CO). Q is the total charge passed during specified time.

Flow cell measurements

Typically, the gas diffusion electrode loaded with Sn-NMC-1000 (GDE, area: 1 cm × 1 cm), a commercial RuO_2 electrode, and Ag/AgCl (saturated KCl) electrode are used as the working electrode, counter electrode, and reference electrode, respectively. An anionic exchange membrane (FAB-PK-130) was used to separate the anolyte and catholyte chamber, while the working electrode was placed between the CO_2 gas chamber and the electrolyte chamber. 1 M KOH was used as the electrolyte to improve the overall reaction efficiency, which was circulated in the cathode chamber by a peristaltic pump at a rate of 20 mL min^{-1} to accelerate mass transfer. CO_2 gas was directly fed to the GDE surface at a flow rate of 18 sccm, and then introduced into the online gas chromatography.

Characterization

The powder X-ray diffraction (XRD) patterns was performed on a Bruker D8 diffractometer (Bruker Corporation, Karlsruhe, Germany) with Cu Kα radiation (λ = 0.15418 nm). Scanning electron microscopy (SEM) was conducted using a Gemini SEM 300 electron microscope (Carl Zeiss AG, Oberkochen, Germany) at an acceleration voltage of 3 kV. Transmission electron microscopy (TEM) images were conducted on a JEM-2100F. An aberration-corrected HAADF-STEM measurement was performed at a JEM-ARF300F. X-ray photoelectron spectroscopy (XPS) analyses were performed by an ESCALAB 250 instrument (Thermo Fisher Scientific, Waltham, Massachusetts, United States). N_2 and CO_2 adsorption–desorption isotherms were conducted on BJ builder Kubo-x1000 instruments (Beijing Builder Electronic Technology Co., Ltd, Beijing, China). The Sn K-edge XAFS spectra was executed at the 1W2B station of the Shanghai Synchrotron Radiation Facility.

Solar-driven CO_2-H_2O system

The flow cell with a solid–liquid–gas interface was used to construct a solar-driven CO_2-H_2O system, and the Sn-NMC-1000 electrode loaded on carbon paper was used as the working electrode. The solar-to-CO conversion efficiency would be improved with alkaline electrolyte over the whole reaction by suppressing the HER and lowering the reaction energy barrier. A commercial triple-junction GaInP/GaAs/Ge solar cell was used as the only input energy under a 300 W Xe lamp with an AM 1.5 G filter. The corresponding current–voltage (I–V) of the solar cell was collected on a Keithley 2400. The solar-to-CO conversion efficiency can be defined as:

$$ST_{CO} = \frac{\Delta E_{CO} \times J \times FE_{CO}}{P_{solar}} \times 100\% \quad (3)$$

where ΔE_{CO} is the equilibrium potential for CO_2 conversion to CO, FE_{CO} is the Faradaic efficiency for CO production, J is the operating current density of the work system, and P_{solar} is the power of input sunlight density (100 mW cm^{-2}).

Computational methods

By using DMol^3 in Material Studio, all DFT calculations were performed with the plane-wave pseudopotential method for the first principle-based quantum mechanics simulations. The generalized gradient approximation within the Perdew–Burke–Ernzerhof form was used as an exchange-correlation function. A Γ-centered Monkhorst–Pack k-point mesh of (3 × 3 × 1) was applied throughout the calculations. A Gaussian smearing finite-temperature broadening method (=0.005 Hatree) was used during structural optimizations and Kohn–Sham self-consistent field calculations were performed with a convergence tolerance of 1×10^{-6} Hatree on the total energy. A 6 × 6 × 1

DOI: 10.31635/ccschem.022.202202464
Citation: *CCS Chem.* **2023**, 5, 2415–2425
Link to VoR: https://doi.org/10.31635/ccschem.022.202202464

super cell graphene with a vacuum layer of 15 Å was used to simulate the catalyst surface. The DFT-D3 correction method of Grimme was used to describe the van der Waals interactions. During computation, the double numerical plus polarization functions (DNP) were used as the basis set with an orbital cutoff of 4.4 Å. *K*-point grids of 3 × 3 × 2 were used for the density of states (DOSs) calculations of all structures.

Results and Discussion

The synthesis process of N_2-Sn-O_2 moieties confined in the three-dimensional carbon nanofiber networks is illustrated in Figure 1a. Typically, the carbon fibers were prepared with the addition of H_2O_2 to trigger the in situ polymerization of aniline and the oxidation of Sn^{2+} ions (Supporting Information Figure S2). XRD patterns and XPS spectra (Supporting Information Figures S3 and S4) confirm the formation of polyaniline and SnO_2 with increasing content of Sn^{2+} ions. The subsequent pyrolysis under N_2 led to the formation of porous carbon due to the release of gases during the polyaniline carbonization. SnO_2 could be converted into atomically dispersed tin atoms through carbothermal reduction and trap the residual oxygen via the coordination effect. SEM and TEM images show that the 3D network structures of interconnected fibers without obvious particles on the surface (Figure 1b,c) can favorably accelerate charge and mass transport to improve the electrocatalysis. The aberration-corrected HAADF-STEM of Sn-NMC-1000 reveals that the atomic-level dispersions of Sn atoms (Figure 1d) and the corresponding energy-distribution X-ray spectroscopy results show the uniform distributions of N, O, and Sn elements in the carbon matrix (Figure 1e). The Sn content of Sn-NMC-1000 examined by the inductively coupled plasma optical emission spectrometry is about 0.24%. Additionally, carbon fibers with similar morphologies (Supporting Information Figure S5) were obtained by changing the temperature from 900 to 1100 °C and were denoted as NMC-1000, Sn-NMC-900, and Sn-NMC-1100. The broad XRD diffraction peaks (Supporting Information Figure S6) at about 25° are indexed to the graphitic carbon, whereas the absence of tin-related diffraction is attributed to the atomic dispersion of metal species in the carbon support.[32–34] In contrast, several sharp diffraction peaks of metallic tin (JCPDS No. 04-0673) are detected as the addition of $SnCl_2$ increased from 0.05 to 0.5 mmol (Supporting Information Figure S7).[35] Meanwhile, large smooth spheres with diameters of ~2 μm are observed on the fiber surface (Supporting Information Figure S8), possibly due to the aggregation of metallic tin at high temperatures. The N_2 adsorption–desorption isotherm curves (Supporting Information Figure S9) show typical I isotherms for all samples, indicating the presence of

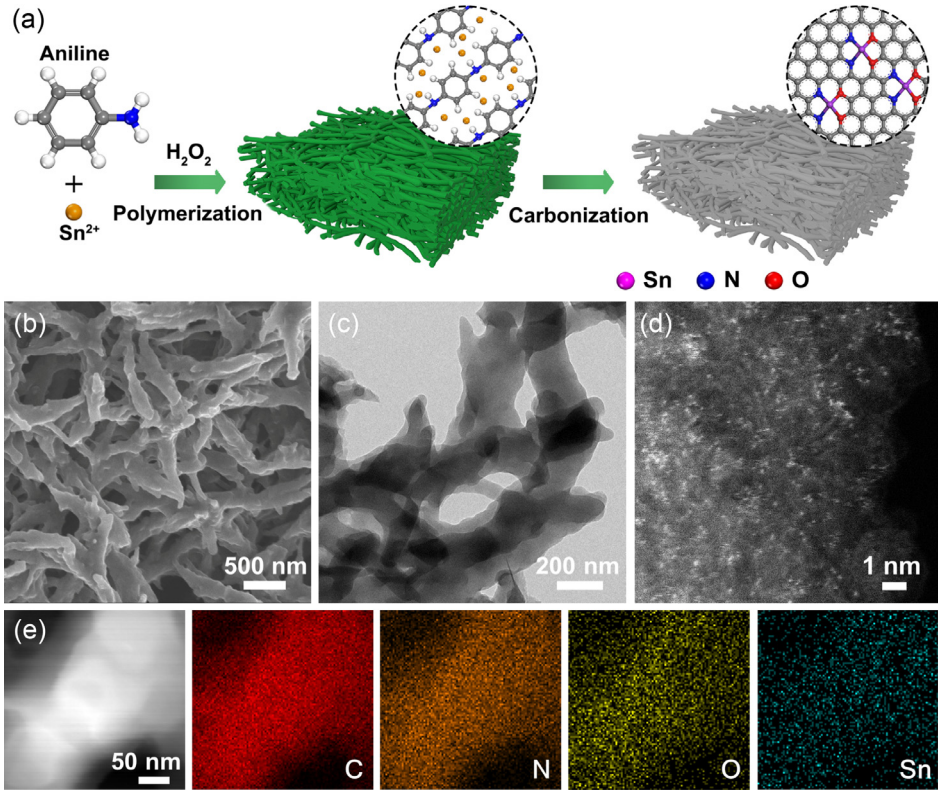

Figure 1 | *(a) Schematic illustration for the preparation of Sn-NMC-1000. (b) SEM, (c) TEM, (d) HAADF-STEM images and (e) the corresponding element mapping images of Sn-NMC-1000.*

DOI: 10.31635/ccschem.022.202202464
Citation: *CCS Chem.* **2023**, 5, 2415–2425
Link to VoR: https://doi.org/10.31635/ccschem.022.202202464

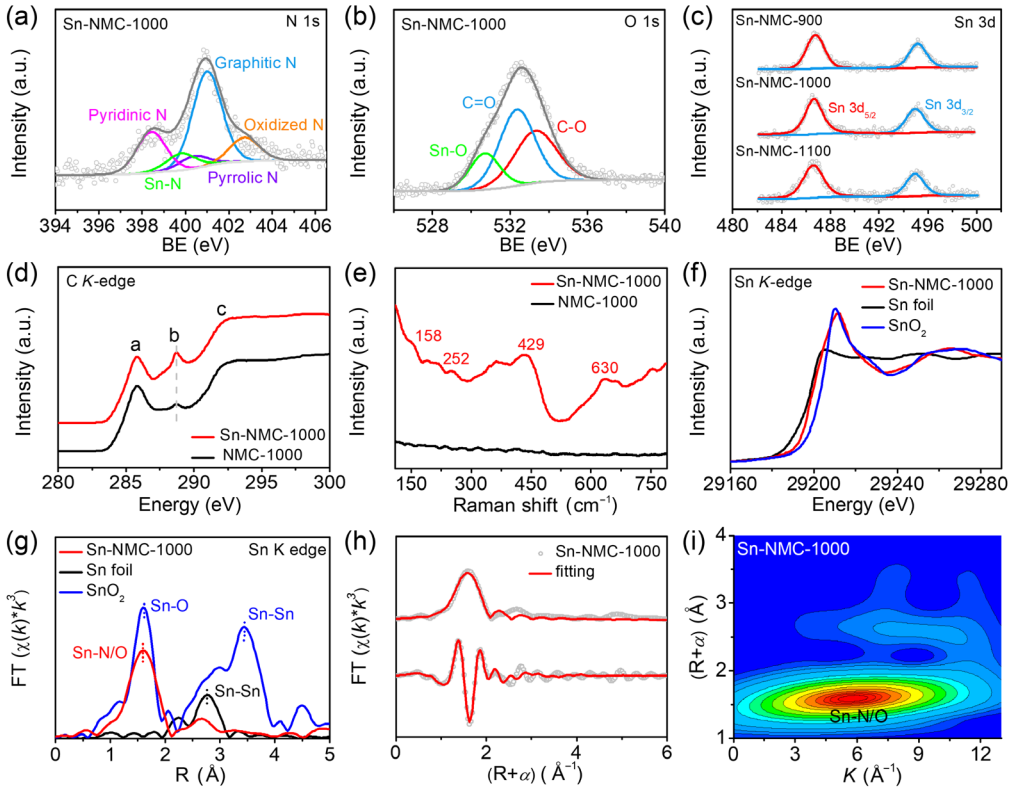

Figure 2 | *High-resolution (a) N 1s and (b) O 1s XPS spectra of Sn-NMC-1000. (c) Sn 3d XPS spectra of Sn-NMC-900, Sn-NMC-1000, and Sn-NMC-1100. (d) C K-edge XANES spectra of Sn-NMC-1000 and NMC-1000. (e) Sectional micro-Raman spectrum of Sn-NMC-1000 and NMC-1000. (f) Sn K-edge XANES spectra and (g) the corresponding Fourier transformed (FT) k^3-weight EXAFS spectra of Sn, SnO_2, and Sn-NMC-1000. (h) The fitting curve of k^3-weight EXAFS spectra. (i) The WT plot of Sn-NMC-1000.*

abundant microporous structures. The largest surface area of Sn-NMC-1000 (471.6 m^2 g^{-1}) is favorable to exposing more active sites for electrocatalysis.

XPS measurements were performed to examine the chemical composition and surface states. The high-resolution N 1s spectra (Figure 2a) of Sn-NMC-1000 reveals the presence of pyridinic (398.4 eV), pyrrolic (400.4 eV), graphitic (401 eV), oxidized nitrogen (402.8 eV), and coordinated nitrogen with metal atom (399.7 eV), suggesting the successful doping of nitrogen with the formation of the Sn-N structure.[23,36,37] Furthermore, graphitic nitrogen is the dominant component when the temperature increases from 900 to 1000 °C (Supporting Information Figure S10), indicating the crucial role of temperature in regulating nitrogen species. The O 1s spectra (Figure 2b and Supporting Information Figure S11) could be fitted into three peaks with binding energies of 530.7, 532.4, and 533.4 eV, corresponding to Sn–O, C=O, and C–O, respectively. Specifically, Sn-NMC-1000 displays a high tin-oxygen content of 18.5%, possibly indicating the capture of abundant oxygen atoms with tin and nitrogen atoms. The high-resolution Sn 3d XPS spectra (Figure 2c) show two apparent peaks with binding energies of ~486.7 and ~495.2 eV corresponding to Sn $3d_{5/2}$ and Sn $3d_{3/2}$, respectively, which are higher than that of Sn^0 (484.7 eV) and lower than that of Sn^{4+} (487.1 eV), illustrating the average valance state of $Sn^{\delta+}$ ($0 < \delta < 4$) in the Sn-NMC-T samples.[27,38] The soft X-ray absorption near-edge structure (XANES) of C K-edge spectrum (Figure 2d) exhibits the similar peaks located at 285.8, 288.7, and 292.2 eV, attributable to the π*C=C, π*C–N, and σ*C–C antibonding orbitals, respectively.[39,40] Notably, the stronger peak b in Sn-NMC-1000 is ascribed to the fingerprint of the sp^3 interaction, revealing the strong interaction between Sn atom and nitrogen-doped carbon.[41,42] For the Sn-NMC-1000 samples, the Raman peaks (Figure 2e) located at 158, 252, 429, and 630 cm^{-1} further confirm the presence of the Sn-N structure.[29] Additionally, two prominent peaks centered at 1317 and 1600 cm^{-1} are attributed to the defective (D band) and graphitic (G band) carbon, respectively (Supporting Information Figure S12). The intensity ratio of the D band over the G band for Sn-NMC-T increases from 0.94 to 0.97 with increasing pyrolysis temperature from 900 to 1100 °C, indicating the formation of a defect-rich structure in the pyrolysis process.[23]

DOI: 10.31635/ccschem.022.202202464
Citation: *CCS Chem.* **2023**, 5, 2415–2425
Link to VoR: https://doi.org/10.31635/ccschem.022.202202464

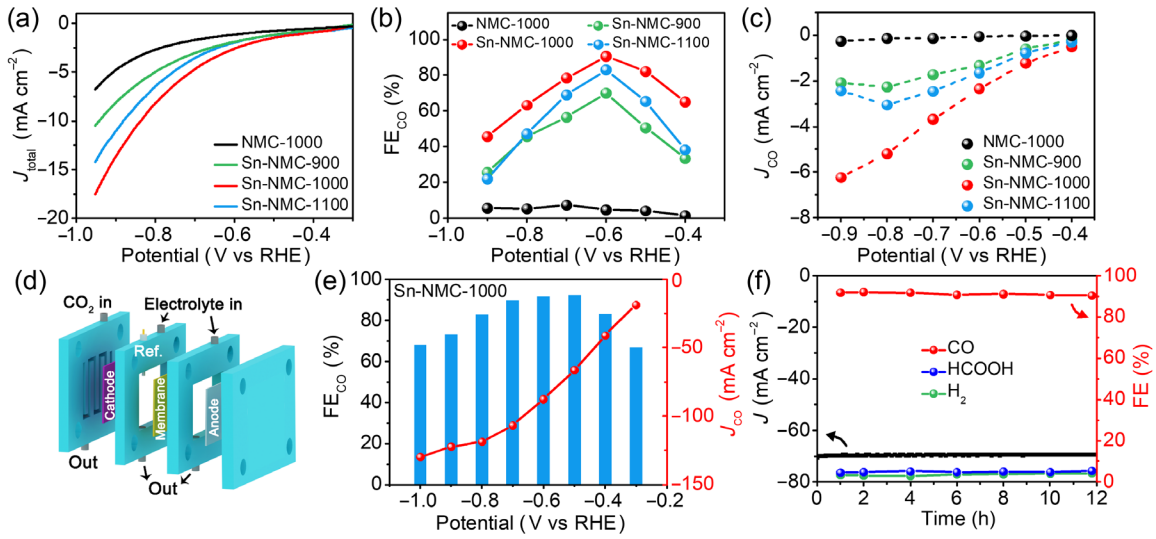

Figure 3 | *(a) LSV curves, (b) CO Faradaic efficiency, (c) CO partial current density at NMC-1000, Sn-NMC-900, Sn-NMC-1000, and Sn-NMC-1100 in the H-type cell, respectively. (d) Schematic illustration of a flow cell. (e) The partial current density and the corresponding FE for CO. (f) Long-term stability test of Sn-NMC-1000 at −0.5 V in a flow cell.*

To examine the chemical state and local coordination of Sn atoms, XANES (Figure 2f) spectra reveal that the absorption edge between Sn foil and SnO_2 suggests the positive valence state of Sn atoms is located between 0 and +4, which is consistent with the XPS results. From the Fourier transform extended X-ray absorption fine structure (FT-EXAFS) oscillations (Figure 2g), a dominant peak at 1.59 Å for Sn-NMC-1000 in comparison with Sn foil and SnO_2 is attributed to the Sn-N/O path at the first shell and the absence of the Sn–Sn bond at 2.77 Å suggests the atomic distribution of Sn atoms. The quantitative coordination of Sn atom was fitted with the bond distances of Sn-N and Sn-O in accordance with the N_2-Sn-O_2 model (Figure 2h and Supporting Information Figure S13 and Table S1). To the best of our knowledge, such a unique coordination structure of Sn-NMC-1000 is identified on the basis of experimental results for the first time. In addition, the EXAFS wavelet transform (WT) plots (Figure 2i and Supporting Information Figure S14) of Sn-NMC-1000 display a remarkable signal of Sn-N/O at 6 Å^{-1} for Sn-NMC-1000 in comparison with Sn foil and SnO_2, further confirming the formation of Sn-N/O configuration. Therefore, the isolated dispersion of N_2-Sn-O_2 in Sn-NMC-1000 would optimize the electronic structure for improved electrocatalytic activity.

Linear sweep voltammetry (LSV) was performed in CO_2- and N_2-saturated 0.5 M $KHCO_3$ to examine the electrocatalytic CO_2RR performance. All the electrodes exhibit higher current density in CO_2-saturated electrolyte in comparison with N_2-saturated one, indicating the favorable reaction kinetics of CO_2RR (Supporting Information Figure S15). Notably, Sn-NMC-1000 exhibits the highest current density in comparison with other electrodes (Figure 3a), indicating the improved catalytic activity. Potential-dependent electrolysis was conducted to identify the possible reduction products. With trace amounts of HCOOH and H_2 (Figure 3b and Supporting Information Figure S16), the CO Faradaic efficiency (FE_{CO}) at the Sn-NMC-1000 electrode exhibits a volcano-like tendency to a maximum value of 90.5% with gradually increasing potential from −0.4 V, illustrating good product selectivity. In contrast, the corresponding FE_{CO} values at the NMC-1000, Sn-NMC-900, and Sn-NMC-1100 electrodes are only 4.7%, 70%, and 83%. For 0.25Sn-NMC-1000 and 0.5Sn-NMC-1000, the increased Sn content does not improve the FE_{CO} for carbon dioxide reduction (Supporting Information Figure S17), possibly due to the loss of active sites along with the aggregation into large Sn spheres. Notably, the current density of Sn-NMC-1000 increased almost linearly with potential from −0.4 V (Figure 3c and Supporting Information Figure S18) to the maximum CO current density of ~6 mA cm^{-2} at −0.9 V, indicating enhanced CO_2RR performance.

Isothermal adsorption for CO_2 was conducted to explore the origin of the excellent electrocatalytic performance (Supporting Information Figure S19). The maximum adsorption amount (36.7 cm^3 g^{-1}) of Sn-NMC-1000 in comparison with those of Sn-NMC-900 (34.7 cm^3 g^{-1}), Sn-N-NMC-1100 (31.8 cm^3 g^{-1}), and NMC-1000 (28.5 cm^3 g^{-1}) suggests the largest surface area for adsorption to improve eletrocatalytic performance,[12] which is mainly attributed to the highly porous structure. To evaluate the reaction kinetics of CO_2RR (Supporting Information Figure S20), the Tafel slope was calculated to be 130 mV dec^{-1} at the Sn-NMC-1000 electrode,

DOI: 10.31635/ccschem.022.202202464
Citation: *CCS Chem.* **2023**, 5, 2415–2425
Link to VoR: https://doi.org/10.31635/ccschem.022.202202464

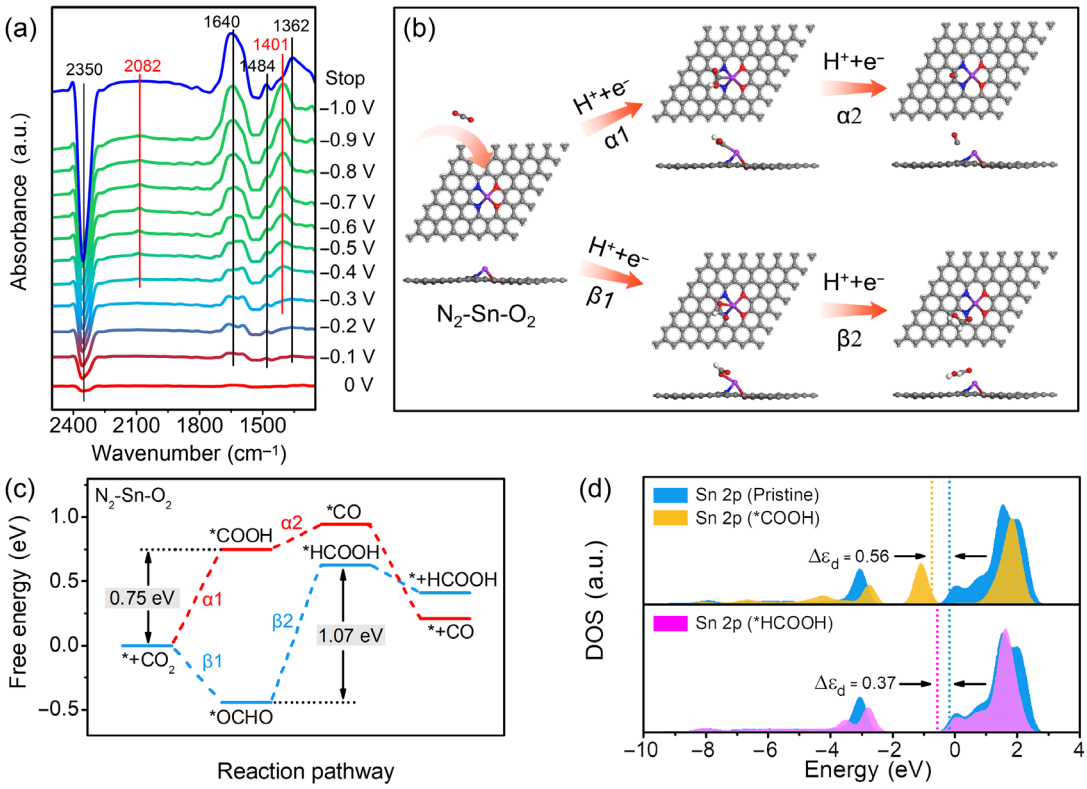

Figure 4 | *(a) Time-dependent ATR-IR spectra for Sn-NMC-1000. (b) Simulation considering reaction pathways for CO and HCOOH generation, respectively. (c) Calculated Gibbs free energy diagrams for CO_2 to CO and HCOOH conversion, respectively. (d) Projected electron DOS of the N_2-Sn-O_2 structure before and after *COOH or *HCOOH interaction.*

much lower than those at Sn-NMC-900 (214 mV dec^{-1}), Sn-NMC-1100 (172 mV dec^{-1}) and NMC-1000 (269 mV dec^{-1}), indicating favorable reaction kinetic process.[43] From the EIS results (Supporting Information Figure S21), the smallest semicircle radius of Sn-NMC-1000 indicates the lowest interfacial charge-transfer resistance due to the fast electron transfer of the interconnected carbon fiber networks. The ECSA are calculated based on the C_{dl} (Supporting Information Figure S22), where the highest C_{dl} value for Sn-NMC-1000 (13 mF cm^{-2}), in comparison with those of Sn-NMC-900 (4.4 mF cm^{-2}), Sn-NMC-1100 (6.8 mF cm^{-2}), and NMC-1000 (3 mF cm^{-2}), confirms the increased electrochemically active sites involved in CO_2RR.

A flow cell with a gas–liquid–solid interface was constructed to address low CO_2 solubility in the electrolyte and mass transport limitations (Figure 3d). The polarization curve of Sn-NMC-1000 in 1 M KOH displays the remarkably low onset potential of ~−0.2 V in comparison with that in an H-shaped one, which is close to the theory equilibrium potential for CO generation. More importantly, the current density is increased to about ~240 mA cm^{-2} at −1.2 V due to the improved CO_2 diffusion, indicating the promising industrial level applications (Supporting Information Figure S23). Sn-NMC-1000 exhibits the enhanced FE_{CO} of 92.1% at −0.5 V probably due to the suppressed HER and improved overall reaction efficiency in the high concentration of alkaline electrolyte, outperforming most of the state-of-the-art Sn-based electrocatalysts (Figure 3e and Supporting Information Figure S24 and Table S2). In addition, the electrochemical stability is an important indicator for the evaluation of practical applications, and no obvious current density decay is observed at the Sn-NMC-1000 electrode during the stability test with an average FE_{CO} of 92%, and no significant change of morphology and composition is detected in comparison with the pristine electrode, manifesting the good electrocatalytic activity and structural stability (Figure 3f and Supporting Information Figure S25).

In situ attenuated total reflection-infrared spectroscopy (ATR-IR) was explored to investigate the reaction pathway of CO production on Sn-NMC-1000 (Figure 4a). In addition to the characteristic peak of the adsorbed CO_2 at 2350 cm^{-1}, the peaks of HCO_3^-, H_2CO_3, and interfacial H_2O at 1362, 1484, and 1640 cm^{-1} respectively,[44] increase gradually and stabilize from −0.3 V to a more negative potential, which is attributed to the rapid equilibrium between CO_2 and HCO_3^-.[45] Specifically, the peak at 1401 cm^{-1} corresponding to the adsorbed *COOH is enhanced from −0.4 V, suggesting the rapid protonation of

DOI: 10.31635/ccschem.022.202202464
Citation: *CCS Chem.* **2023**, 5, 2415–2425
Link to VoR: https://doi.org/10.31635/ccschem.022.202202464

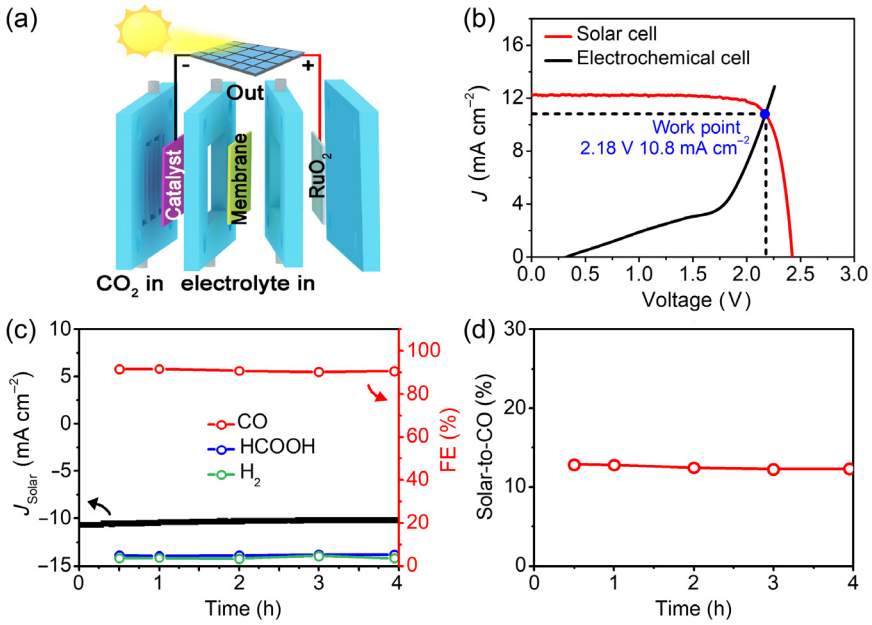

Figure 5 | *(a) Schematic illustration of the solar-driven CO_2-H_2O splitting system. (b) I–V curves of photovoltaic under irradiation and electrolysis cell. (c) The stability test with current density and corresponding Faradaic efficiency for the solar-driven CO_2 reduction. (d) Solar-to-CO conversion efficiency.*

$CO_2^{\bullet-}$ via the proton-coupled electron transfer steps.[19] The peak at 2082 cm^{-1} attributable to the linearly bonded CO (CO_L) is detected from −0.4 V, consistent with the onset potential of CO generation (Figure 3b).[46] Specifically, the immediate absence of peaks for *COOH and *CO during the potential rest further confirms the formation of such intermediates during CO_2RR. Thus, the presence of the N_2-Sn-O_2 structure would regulate the surface chemical status and promote the electrochemical conversion of CO_2 into CO.

The general Sn-N-C structures reported enable the electrocatalytic CO_2 reduction to formate as the main product, but the selective CO generation via regulating the coordination structure and surface electronic properties is rare. To gain insight into the good activity and selectivity of N_2-Sn-O_2 in the electrocatalytic reduction of CO_2, DFT calculations were performed to examine two main pathways for the production of CO and formate on the optimized N_2-Sn-O_2 structures in different states (Figure 4b and Supporting Information Figure S26). From the free energy diagram (Figure 4c), the formation of *OCHO is easy due to the down-hill free energy pathway in comparison with *COOH, but the subsequent protonation process is severely inhibited due to the increased energy barrier. In contrast, the smaller energy barrier required for the formation of CO is favorable for the whole catalytic process. It should be noted that the presence of N_2-Sn-O_2 leads to a significant change in the overall reaction pathway, lowering the energy barrier of 1.07 eV for the rate determination step of HCOOH generation and 0.75 eV for CO generation. Thus, the selectivity is improved, possibly due to the distinct changes in the electronic structure for the adsorption process. Additionally, the generated *CO on the N_2-Sn-O_2 surface could be easily desorbed without poisoning the active sites, in accordance with the in situ ATR-IR results. The electronic interplay between N_2-Sn-O_2 and intermediates (e.g., *HCOOH, *COOH) was further investigated by the projected DOS (Figure 4d). The N_2-Sn-O_2 structure before and after interaction with *COOH shows the significant change in the d-band center of the Sn 2p orbital in comparison with the interacting *HCOOH, and the obvious charge delocalization between the Sn 2p orbital of N_2-Sn-O_2 and the antibonding C 2p orbital of *COOH[47] would facilitate and stabilize *COOH to produce CO rather than HCOOH. Therefore, different from the normal metal-nitrogen-carbon structures, the oxygen species in the N_2-Sn-O_2 structure would significantly change the electronic structure to modulate the intermediate adsorption process and accelerate the proton-coupled electron transfer for CO generation.

Benefiting from the excellent CO_2RR performance of Sn-NMC-1000, the CO_2-H_2O overall splitting system in 1 M KOH electrolyte was constructed using a solar cell as the only input energy (Figure 5a and Supporting Information Figure S27). The GaInP/GaAs/Ge cell displays the open-circuit voltage and short-circuit current is 2.42 V and 12.3 mA cm^{-2}, respectively, under solar irradiation. The working potential and current density of the system can be determined by the intersection of the

DOI: 10.31635/ccschem.022.202202464
Citation: *CCS Chem.* **2023**, 5, 2415–2425
Link to VoR: https://doi.org/10.31635/ccschem.022.202202464

I–V curves of the electrochemical cell and solar cell via catalyst loading optimization (Figure 5b). At a potential of 2.18 V, the solar-driven CO_2-H_2O system displays a current density of 10.3 mA cm^{-2} with an average FE_{CO} over 90% during the operation process, illustrating the good selectivity and catalytic activity (Figure 5c). More importantly, the high solar-to-CO conversion efficiency of 12.9% can be achieved (Figure 5d). This work provides a promising strategy to couple solar and chemical energy to achieve the effective recycling of renewable energy.

Conclusion

In summary, the tin single-atom with unique atomic bridging structure confined in a porous carbon fiber was synthesized by a one-step carbonization strategy. The x-ray absorption spectroscopy (XAS) and HAADF-STEM results revealed that the coordination of oxygen with the metal-nitrogen-carbon led to the formation of novel atomic bridging structure of N_2-Sn-O_2. The resultant electrocatalyst exhibited good catalytic activity and selectivity for CO generation with a high Faradaic efficiency of 92.1% and large current density over 240 mA cm^{-2}, different from the generally reported Sn-based electrocatalysts for formate generation. The combination of in-situ experimental results and theoretical calculation demonstrated that the modification of metal-nitrogen-carbon with coordinated oxygen in the interconnected carbon fiber networks with fast electron transport can efficiently regulate the surface electronic structure to improve the electrocatalytic activity and selectivity. Additionally, the integrated CO_2-H_2O splitting system composed of Sn-NMC-1000 electrocatalyst displayed high solar-to-CO conversion efficiency. This work reveals the conformational relationship between the coordination structure and catalytic performance, providing basic guidance for the design of unique atomic structure to achieve good electrocatalytic activity.

Supporting Information

Supporting Information is available and includes the experimental results: SEM, TEM, XRD, XPS, Brunauer–Emmett–Teller (BET), Raman, EXAFS, LSV, FEs, EIS, ECSA, and the performance comparison.

Conflict of Interest

There is no conflict of interest to report.

Funding Information

This work was financially supported by the National Natural Science Foundation of China (grant no. 22175108), the Natural Scientific Foundation (grant nos. ZR2020JQ09 and ZR2022ZD27) of Shandong Province, and the Taishan Scholars Program of Shandong Province, Project for Scientific Research Innovation Team of Young Scholar in Colleges, Universities of Shandong Province (grant no. 2019KJC025). The authors also acknowledge the assistance of the Analytical Center for Structural Constituent and Physical Property of Core Facilities Sharing Platform, Shandong University.

References

1. Ma, W.; Xie, S.; Liu, T.; Fan, Q.; Ye, J.; Sun, F.; Jiang, Z.; Zhang, Q.; Cheng, J.; Wang, Y. Electrocatalytic Reduction of CO_2 to Ethylene and Ethanol Through Hydrogen-Assisted C–C Coupling over Fluorine-Modified Copper. *Nat. Catal.* **2020**, *3*, 478–487.
2. Yang, H.; Wu, Y.; Lin, Q.; Fan, L.; Chai, X.; Zhang, Q.; Liu, J.; He, C.; Lin, Z. Composition Tailoring via N and S Co-Doping and Structure Tuning by Constructing Hierarchical Pores: Metal-Free Catalysts for High-Performance Electrochemical Reduction of CO_2. *Angew. Chem. Int. Ed.* **2018**, *57*, 15476–15480.
3. Shi, Y.; Ji, Y.; Long, J.; Liang, Y.; Liu, Y.; Yu, Y.; Xiao, J.; Zhang, B. Unveiling Hydrocerussite as an Electrochemically Stable Active Phase for Efficient Carbon Dioxide Electroreduction to Formate. *Nat. Commun.* **2020**, *11*, 3415.
4. Han, N.; Ding, P.; He, L.; Li, Y.; Li, Y. Promises of Main Group Metal-Based Nanostructured Materials for Electrochemical CO_2 Reduction to Formate. *Adv. Energy Mater.* **2020**, *10*, 1902338.
5. Liu, K.; Wang, J.; Shi, M.; Yan, J.; Jiang, Q. Simultaneous Achieving of High Faradaic Efficiency and CO Partial Current Density for CO_2 Reduction via Robust, Noble-Metal-Free Zn Nanosheets with Favorable Adsorption Energy. *Adv. Energy Mater.* **2019**, *9*, 1900276.
6. Zhu, Y. T.; Cui, X. Y.; Liu, H. L.; Guo, Z. G.; Dang, Y. F.; Fan, Z. X.; Zhang, Z. C.; Hu, W. P. Tandem Catalysis in Electrochemical CO_2 Reduction Reaction. *Nano Res.* **2021**, *14*, 4471–4486.
7. Schreier, M.; Héroguel, F.; Steier, L.; Ahmad, S.; Luterbacher, J. S.; Mayer, M. T.; Luo, J.; Grätzel, M. Solar Conversion of CO_2 to CO Using Earth-Abundant Electrocatalysts Prepared by Atomic Layer Modification of CuO. *Nat. Energy* **2017**, *2*, 17087.
8. Chen, C.; Yan, X.; Liu, S.; Wu, Y.; Wan, Q.; Sun, X.; Zhu, Q.; Liu, H.; Ma, J.; Zheng, L.; Wu, H.; Han, B. Highly Efficient Electroreduction of CO_2 to C_{2+} Alcohols on Heterogeneous Dual Active Sites. *Angew. Chem. Int. Ed.* **2020**, *59*, 16459–16464.
9. Chen, Z.; Wang, T.; Liu, B.; Cheng, D.; Hu, C.; Zhang, G.; Zhu, W.; Wang, H.; Zhao, Z.-J.; Gong, J. Grain-Boundary-Rich Copper for Efficient Solar-Driven Electrochemical CO_2 Reduction to Ethylene and Ethanol. *J. Am. Chem. Soc.* **2020**, *142*, 6878–6883.
10. Yang, P.-P.; Zhang, X.-L.; Gao, F.-Y.; Zheng, Y.-R.; Niu, Z.-Z.; Yu, X.; Liu, R.; Wu, Z.-Z.; Qin, S.; Chi, L.-P.; Duan, Y.; Ma,

DOI: 10.31635/ccschem.022.202202464
Citation: *CCS Chem.* **2023**, 5, 2415–2425
Link to VoR: https://doi.org/10.31635/ccschem.022.202202464

T.; Zheng, X.-S.; Zhu, J.-F.; Wang, H.-J.; Gao, M.-R.; Yu, S.-H. Protecting Copper Oxidation State via Intermediate Confinement for Selective CO_2 Electroreduction to C_{2+} Fuels. *J. Am. Chem. Soc.* **2020**, *142*, 6400–6408.
11. Huang, M.; Gong, S.; Wang, C.; Yang, Y.; Jiang, P.; Wang, P.; Hu, L.; Chen, Q. Lewis-Basic EDTA as a Highly Active Molecular Electrocatalyst for CO_2 Reduction to CH_4. *Angew. Chem. Int. Ed.* **2021**, *60*, 23002–23009.
12. Cao, X.; Wulan, B.; Zhang, B.; Tan, D.; Zhang, J. Defect Evolution of Hierarchical SnO_2 Aggregates for Boosting CO_2 Electrocatalytic Reduction. *J. Mater. Chem. A* **2021**, *9*, 14741–14751.
13. Zhong, D.; Zhao, Z.-J.; Zhao, Q.; Cheng, D.; Liu, B.; Zhang, G.; Deng, W.; Dong, H.; Zhang, L.; Li, J.; Li, J.; Gong, J. Coupling of Cu(100) and (110) Facets Promotes Carbon Dioxide Conversion to Hydrocarbons and Alcohols. *Angew. Chem. Int. Ed.* **2021**, *60*, 4879–4885.
14. Duan, Y.-X.; Zhou, Y.-T.; Yu, Z.; Liu, D.-X.; Wen, Z.; Yan, J.-M.; Jiang, Q. Boosting Production of HCOOH from CO_2 Electroreduction via Bi/CeO_x. *Angew. Chem. Int. Ed.* **2021**, *60*, 8798–8802.
15. Wang, Y.; Cao, L.; Libretto, N. J.; Li, X.; Li, C.; Wan, Y.; He, C.; Lee, J.; Gregg, J.; Zong, H.; Su, D.; Miller, J. T.; Mueller, T.; Wang, C. Ensemble Effect in Bimetallic Electrocatalysts for CO_2 Reduction. *J. Am. Chem. Soc.* **2019**, *141*, 16635–16642.
16. Shan, W.; Liu, R.; Zhao, H.; He, Z.; Lai, Y.; Li, S.; He, G.; Liu, J. In Situ Surface-Enhanced Raman Spectroscopic Evidence on the Origin of Selectivity in CO_2 Electrocatalytic Reduction. *ACS Nano* **2020**, *14*, 11363–11372.
17. Gao, J.; Zhang, H.; Guo, X.; Luo, J.; Zakeeruddin, S. M.; Ren, D.; Grätzel, M. Selective C–C Coupling in Carbon Dioxide Electroreduction via Efficient Spillover of Intermediates as Supported by Operando Raman Spectroscopy. *J. Am. Chem. Soc.* **2019**, *141*, 18704–18714.
18. Cheng, H.; Wu, X.; Feng, M.; Li, X.; Lei, G.; Fan, Z.; Pan, D.; Cui, F.; He, G. Atomically Dispersed Ni/Cu Dual Sites for Boosting the CO_2 Reduction Reaction. *ACS Catal.* **2021**, *11*, 12673–12681.
19. Wulan, B.; Cao, X.; Tan, D.; Shu, X.; Zhang, J. Atomic Bridging of Metal-Nitrogen-Carbon toward Efficient Integrated Electrocatalysis. *Adv. Funct. Mater.* **2022**, *32*, 2203842.
20. Ni, W.; Gao, Y.; Lin, Y.; Ma, C.; Guo, X.; Wang, S.; Zhang, S. Nonnitrogen Coordination Environment Steering Electrochemical CO_2-to-CO Conversion over Single-Atom Tin Catalysts in a Wide Potential Window. *ACS Catal.* **2021**, *11*, 5212–5221.
21. Chen, D.; Zhang, L.-H.; Du, J.; Wang, H.; Guo, J.; Zhan, J.; Li, F.; Yu, F. A Tandem Strategy for Enhancing Electrochemical CO_2 Reduction Activity of Single-Atom Cu-S_1N_3 Catalysts via Integration with Cu Nanoclusters. *Angew. Chem. Int. Ed.* **2021**, *60*, 24022–24027.
22. Guo, J.; Zhang, W.; Zhang, L.-H.; Chen, D.; Zhan, J.; Wang, X.; Shiju, N. R.; Yu, F. Control over Electrochemical CO_2 Reduction Selectivity by Coordination Engineering of Tin Single-Atom Catalysts. *Adv. Sci.* **2021**, *8*, 2102884.
23. Wang, T.; Sang, X.; Zheng, W.; Yang, B.; Yao, S.; Lei, C.; Li, Z.; He, Q.; Lu, J.; Lei, L.; Dai, L.; Hou, Y. Gas Diffusion Strategy for Inserting Atomic Iron Sites into Graphitized Carbon Supports for Unusually High-Efficient CO_2 Electroreduction and High-Performance Zn–CO_2 Batteries. *Adv. Mater.* **2020**, *32*, 2002430.
24. Yang, F.; Song, P.; Liu, X.; Mei, B.; Xing, W.; Jiang, Z.; Gu, L.; Xu, W. Highly Efficient CO_2 Electroreduction on ZnN_4-Based Single-Atom Catalyst. *Angew. Chem. Int. Ed.* **2018**, *57*, 12303–12307.
25. Zhang, Y.; Jiao, L.; Yang, W.; Xie, C.; Jiang, H.-L. Rational Fabrication of Low-Coordinate Single-Atom Ni Electrocatalysts by MOFs for Highly Selective CO_2 Reduction. *Angew. Chem. Int. Ed.* **2021**, *60*, 7607–7611.
26. Yang, H.; Lin, Q.; Wu, Y.; Li, G.; Hu, Q.; Chai, X.; Ren, X.; Zhang, Q.; Liu, J.; He, C. Highly Efficient Utilization of Single Atoms via Constructing 3D and Free-Standing Electrodes for CO_2 Reduction with Ultrahigh Current Density. *Nano Energy* **2020**, *70*, 104454.
27. Jiang, Z.; Wang, T.; Pei, J.; Shang, H.; Zhou, D.; Li, H.; Dong, J.; Wang, Y.; Cao, R.; Zhuang, Z.; Chen, W.; Wang, D.; Zhang, J.; Li, Y. Discovery of Main Group Single Sb–N_4 Active Sites for CO_2 Electroreduction to Formate with High Efficiency. *Energy Environ. Sci.* **2020**, *13*, 2856–2863.
28. Lei, F.; Liu, W.; Sun, Y.; Xu, J.; Liu, K.; Liang, L.; Yao, T.; Pan, B.; Wei, S.; Xie, Y. Metallic Tin Quantum Sheets Confined in Graphene toward High-Efficiency Carbon Dioxide Electroreduction. *Nat. Commun.* **2016**, *7*, 12697.
29. Zu, X.; Li, X.; Liu, W.; Sun, Y.; Xu, J.; Yao, T.; Yan, W.; Gao, S.; Wang, C.; Wei, S.; Xie, Y. Efficient and Robust Carbon Dioxide Electroreduction Enabled by Atomically Dispersed $Sn^{\delta+}$ Sites. *Adv. Mater.* **2019**, *31*, 1808135.
30. Zheng, W.; Yang, J.; Chen, H.; Hou, Y.; Wang, Q.; Gu, M.; He, F.; Xia, Y.; Xia, Z.; Li, Z.; Yang, B.; Lei, L.; Yuan, C.; He, Q.; Qiu, M.; Feng, X. Atomically Defined Undercoordinated Active Sites for Highly Efficient CO_2 Electroreduction. *Adv. Funct. Mater.* **2020**, *30*, 1907658.
31. Yan, C.; Li, H.; Ye, Y.; Wu, H.; Cai, F.; Si, R.; Xiao, J.; Miao, S.; Xie, S.; Yang, F.; Li, Y.; Wang, G.; Bao, X. Coordinatively Unsaturated Nickel–Nitrogen Sites towards Selective and High-Rate CO_2 Electroreduction. *Energy Environ. Sci.* **2018**, *11*, 1204–1210.
32. Wang, C.; Hu, X.; Hu, X.; Liu, X.; Guan, Q.; Hao, R.; Liu, Y.; Li, W. Typical Transition Metal Single-Atom Catalysts with a Metal-Pyridine N Structure for Efficient CO_2 Electroreduction. *Appl. Catal. B: Environ.* **2021**, *296*, 120331.
33. Zhang, J.; Zhao, Z.; Xia, Z.; Dai, L. A Metal-Free Bifunctional Electrocatalyst for Oxygen Reduction and Oxygen Evolution Reactions. *Nat. Nanotech.* **2015**, *10*, 444–452.
34. Xiao, X.; Li, X.; Wang, Z.; Yan, G.; Guo, H.; Hu, Q.; Li, L.; Liu, Y.; Wang, J. Robust Template-Activator Cooperated Pyrolysis Enabling Hierarchically Porous Honeycombed Defective Carbon as Highly-Efficient Metal-Free Bifunctional Electrocatalyst for Zn-Air Batteries. *Appl. Catal. B Environ.* **2020**, *265*, 118603.
35. Zhang, B.; Sun, L.; Wang, Y.; Chen, S.; Zhang, J. Well-Dispersed SnO_2 Nanocrystals on N-Doped Carbon Nanowires as Efficient Electrocatalysts for Carbon Dioxide Reduction. *J. Energy Chem.* **2020**, *41*, 7–14.

DOI: 10.31635/ccschem.022.202202464
Citation: *CCS Chem.* **2023**, 5, 2415–2425
Link to VoR: https://doi.org/10.31635/ccschem.022.202202464

36. Luo, H.; Jiang, W.-J.; Niu, S.; Zhang, X.; Zhang, Y.; Yuan, L.-P.; He, C.; Hu, J.-S. Self-Catalyzed Growth of Co–N–C Nanobrushes for Efficient Rechargeable Zn–Air Batteries. *Small* **2020**, *16*, 2001171.
37. Zhang, Z.; Sun, J.; Wang, F.; Dai, L. Efficient Oxygen Reduction Reaction (ORR) Catalysts Based on Single Iron Atoms Dispersed on a Hierarchically Structured Porous Carbon Framework. *Angew. Chem. Int. Ed.* **2018**, *57*, 9038–9043.
38. Zhao, C.; Dai, X.; Yao, T.; Chen, W.; Wang, X.; Wang, J.; Yang, J.; Wei, S.; Wu, Y.; Li, Y. Ionic Exchange of Metal–Organic Frameworks to Access Single Nickel Sites for Efficient Electroreduction of CO_2. *J. Am. Chem. Soc.* **2017**, *139*, 8078–8081.
39. Jiang, K.; Siahrostami, S.; Zheng, T.; Hu, Y.; Hwang, S.; Stavitski, E.; Peng, Y.; Dynes, J.; Gangisetty, M.; Su, D.; Attenkofer, K.; Wang, H. Isolated Ni Single Atoms in Graphene Nanosheets for High-Performance CO_2 Reduction. *Energy Environ. Sci.* **2018**, *11*, 893–903.
40. Tong, Y.; Chen, P.; Zhou, T.; Xu, K.; Chu, W.; Wu, C.; Xie, Y. A Bifunctional Hybrid Electrocatalyst for Oxygen Reduction and Evolution: Cobalt Oxide Nanoparticles Strongly Coupled to B,N-Decorated Graphene. *Angew. Chem. Int. Ed.* **2017**, *56*, 7121–7125.
41. Jiang, Z.; Sun, W.; Shang, H.; Chen, W.; Sun, T.; Li, H.; Dong, J.; Zhou, J.; Li, Z.; Wang, Y.; Cao, R.; Sarangi, R.; Yang, Z.; Wang, D.; Zhang, J.; Li, Y. Atomic Interface Effect of a Single Atom Copper Catalyst for Enhanced Oxygen Reduction Reactions. *Energy Environ. Sci.* **2019**, *12*, 3508–3514.
42. Zheng, X.; De Luna, P.; García de Arquer, F. P.; Zhang, B.; Becknell, N.; Ross, M. B.; Li, Y.; Banis, M. N.; Li, Y.; Liu, M.; Voznyy, O.; Dinh, C. T.; Zhuang, T.; Stadler, P.; Cui, Y.; Du, X.; Yang, P.; Sargent, E. H. Sulfur-Modulated Tin Sites Enable Highly Selective Electrochemical Reduction of CO_2 to Formate. *Joule* **2017**, *1*, 794–805.
43. Duan, Y.-X.; Liu, K.-H.; Zhang, Q.; Yan, J.-M.; Jiang, Q. Efficient CO_2 Reduction to HCOOH with High Selectivity and Energy Efficiency over Bi/rGO Catalyst. *Small Methods* **2020**, *4*, 1900846.
44. Deng, W.; Zhang, L.; Li, L.; Chen, S.; Hu, C.; Zhao, Z.-J.; Wang, T.; Gong, J. Crucial Role of Surface Hydroxyls on the Activity and Stability in Electrochemical CO_2 Reduction. *J. Am. Chem. Soc.* **2019**, *141*, 2911–2915.
45. Cao, X.; Zhao, L.; Wulan, B.; Tan, D.; Chen, Q.; Ma, J.; Zhang, J. Atomic Bridging Structure of Nickel–Nitrogen–Carbon for Highly Efficient Electrocatalytic Reduction of CO_2. *Angew. Chem. Int. Ed.* **2022**, *61*, e202113918.
46. Huo, S. J.; Xue, X. K.; Yan, Y. G.; Li, Q. X.; Ma, M.; Cai, W. B.; Xu, Q. J.; Osawa, M. Extending in Situ Attenuated-Total-Reflection Surface-Enhanced Infrared Absorption Spectroscopy to Ni Electrodes. *J. Phys. Chem. B* **2006**, *110*, 4162–4169.
47. Li, S.; Zhao, S.; Lu, X.; Ceccato, M.; Hu, X.-M.; Roldan, A.; Catalano, J.; Liu, M.; Skrydstrup, T.; Daasbjerg, K. Low-Valence $Zn^{\delta+}$ ($0<\delta<2$) Single-Atom Material as Highly Efficient Electrocatalyst for CO_2 Reduction. *Angew. Chem. Int. Ed.* **2021**, *60*, 22826–22832.

DOI: 10.31635/ccschem.022.202202464
Citation: *CCS Chem.* **2023**, 5, 2415–2425
Link to VoR: https://doi.org/10.31635/ccschem.022.202202464